

Sparsity Weak Lensing 3-D Density Map Reconstruction

ABSTRACT

A new method is developed to reconstruct 3-D density contrast fields from photometric weak lensing shear measurements. The 3-D density contrast map is modeled as a superposition of basis atoms. The basis atoms are designed to represent the structure of NFW halos which have 2-D multi-scale NFW surface density profiles on the transverse plane and 1-D Dirac delta functions in the line-of-sight direction. With the prior assumption that the basis atoms have a sparse distribution, the density field is reconstructed using the adaptive lasso algorithm. The method is tested with realistic simulation using HSC-like shape noise and photo- z uncertainties. **Add descriptions on the outcomes of the test on the simulations.**

1. INTRODUCTION

Light from distant galaxies is distorted by the intervening inhomogeneous density distribution along the line-of-sight due to the influence of gravity. As a result of the light distortion, the shapes of the background galaxies are coherently sheared. Such effect, which is known as weak lensing, imprints the information of foreground mass density distribution to the background galaxy images and offers a direct probe into the mass density distribution in our universe (see [Kilbinger 2015](#); [Mandelbaum 2018](#), for recent reviews).

Adopting the thin lens approximation, the expected shear measurements (γ) on distant galaxies are related to the foreground density contrast field (δ) through a linear transformation

$$\gamma = \mathbf{T}\delta, \quad (1)$$

where \mathbf{T} is used to denote the linear transformation operator which includes not only physical lensing effect but also includes observational systematic effects from the observation (e.g. pixelization and smoothing of shear field in transverse plane, photo- z uncertainties).

Several large scale surveys target to study the weak lensing effect at high precision level (e.g. HSC ([Aihara et al. 2018](#)), KIDS ([de Jong et al. 2013](#)), DES ([The Dark Energy Survey Collaboration 2005](#)), LSST ([LSST Science Collaboration et al. 2009](#)), Euclid ([Laureijs et al. 2011](#)), WFIRST ([Spergel et al. 2015](#))).

The primary goal of most weak lensing surveys is to constrain the cosmology model through 2-point correlations. The studies include galaxy-galaxy lensing which cross correlating the shear field (γ) with the positions of foreground galaxies ([Han et al. 2015](#); [More et al. 2015](#); [Prat et al. 2018](#)), and cosmic shear which auto-correlates the shear measurements ([Morrison et al. 2016](#); [Troxel et al. 2018](#); [Hikage et al. 2019](#); [Hamana et al. 2020](#)).

Since shear is directly related to the matter distribution as shown in eq. (1), Galaxy-galaxy lensing probes into the correlation between the matter field and galaxy field, on the other hand, cosmic shear probes into the auto-correlation of matter field.

Reconstructions of density map from shear measurements also receive considerable interest. 2-D density map reconstruction which reconstructs the integration of mass along the line-of-sight direction has been well studied by the community ([Kaiser & Squires 1993](#); [Lanusse et al. 2016](#)) and applied to large scale surveys ([Oguri et al. 2018](#); [Chang et al. 2018](#); [Jeffrey et al. 2018](#)).

In order to fully reconstruct the 3-D mass density distribution (δ) from the tomographic shear observations (γ), the density contrast field is modeled as a superposition of basis atoms in a dictionary space

$$\delta = \Phi x, \quad (2)$$

where Φ is the transformation operator from the parameters in the dictionary space to the density contrast and x denotes the parameters in the dictionary space. [Simon et al. \(2009\)](#) reconstruct the density field in Fourier space, which is equivalent to model the mass field with sinusoidal functions. On the other hand, [Leonard et al. \(2014\)](#) models the mass field with Starlets.

The model parameters are estimated through solving an optimization problem and the estimator is defined as

$$\hat{x} = \arg \min_x \left\{ \frac{1}{2} \left\| \Sigma^{-\frac{1}{2}} (\gamma - \mathbf{T}\Phi x) \right\|_2^2 + \lambda C(x) \right\}, \quad (3)$$

where $\left\| \Sigma^{-\frac{1}{2}} (\gamma - \mathbf{T}\Phi x) \right\|_2^2$ is the chi-square term¹ measuring the residuals between the prediction and the data,

¹ weighted by the inverse of the diagonal covariance matrix of error on the shear measurements (Σ).

while $C(x)$ is the regularization term measuring the deviation of the estimation of the parameter (x) from the prior assumptions. Such estimation prefer the parameters that are able to describe the observations and also align with the prior assumptions. The regularization parameter λ adjusts the relative weight between the observations and prior assumptions in the optimization process.

Simon et al. (2009) propose to use the l^2 ridge regulation ($C = \|x\|_2^2$) to find the best-fit solution in Fourier space. Oguri et al. (2018) apply the method of Simon et al. (2009) to the first year data of the Hyper Suprime-Cam Survey (Aihara et al. 2018). **Why we use l^1 in this paper, what is the difference between l^1 and l^2 .**

Leonard et al. (2014) propose to use the l^1 lasso regulation ($C = \|x\|_1$) to find the best-fits solution in a Starlets dictionary space. However, the Starlets functions are not designed to model the clumpy mass distributions in the universe and Leonard et al. (2014) use a greedy descent algorithm to find minima of the loss function, which is not guaranteed to converge to the global minima (cite..).

N -body simulations have shown that the dark matter is distributed in halos connected by filaments, and the density distribution of a halo follows the NFW profile (Navarro et al. 1997). We construct a dictionary which is composed of multi-scale NFW atoms and point mass atoms. The multi-scale NFW atoms are used to model the structures within halos. They follow multi-scale surface density profiles of NFW halos (Takada & Jain 2003) on the transverse plane and Dirac delta function in the line-of-sight direction. By using Dirac delta functions in the line-of-sight direction, the depth of halo is neglected (Leonard et al. 2014) since the resolution scale of the reconstruction in the line-of-sight direction is much larger than the halo scale. The point mass atoms are used to model the structures in the filaments and structures smaller than the reachable resolution on the transverse plane. Furthermore, the point mass atoms make our dictionary space complete. With the prior assumption that the density contrast field is sparse in the dictionary space, the adaptive lasso regularization (Zou 2006) is used to reconstruct a high signal-to-noise-ratio (SNR) density contrast field.

Comparing with Leonard et al. (2014), our dictionary space is built up to describe the clumpy mass in the universe which has clear physical a motivation. Moreover, we use adaptive lasso which does not rely on any greedy descent alorithm, therefore the estimation is guaranteed to converge to the global minimum.

This paper is organized as follows. Section 2 proposes the new method for 3-D density map reconstruction.

Section 3 introduces the realistic simulations we use to test the new method. Section 4 presents the results of our method on the simulations. Section 5 summarizes and discusses the future development of the method.

2. METHODOLOGY

In this section, we first review how foreground density distributions induce weak lensing shear distortions on background galaxies in section 2.1. Then, we introduce the dictionary space used to model the foreground density map in section 2.2.

Subsequently, in section 2.3 we discuss several systematic effects from observations which include photo- z uncertainty (section 2.3.1), smoothing (section 2.3.2), masking(section 2.3.3), and pixelization (section 2.3.4).

Finally, we find the the sparse solution in section 2.4 using the adaptive lasso algorithm (Zou 2006) optimized with the FISTA alorithm (Beck & Teboulle 2009).

2.1. Lensing

The lensing convergence κ at the comoving distance χ_s caused by the foreground inhomogeneous density distribution at the comoving distance χ_l ($\chi_l < \chi_s$) along the line-of-sight is (Leonard et al. 2014)

$$\kappa(\vec{\theta}, \chi_s) = \frac{3H_0^2\Omega_M}{2c^2} \int_0^{\chi_s} d\chi_l \frac{\chi_l \chi_{sl}}{\chi_s} \frac{\delta(\vec{\theta}, \chi_l)}{a(\chi_l)}, \quad (4)$$

where $\delta = \rho(\vec{\theta}, \chi_l)/\bar{\rho} - 1$ is the density contrast at the position of lens, H_0 is the Hubble parameter, Ω_M is the matter density parameter, c is the speed of light, and $a(\chi_l)$ is the scale parameter at the lens position.

Substitute comoving distance (χ) with redshift (z)

$$\kappa(\vec{\theta}, z_s) = \int_0^{z_s} dz_l K(z_l, z_s) \delta(\vec{\theta}, z_l). \quad (5)$$

where $K(z_l, z_s)$ is the lensing kernel defined as

$$K(z_l, z_s) = \begin{cases} \frac{3H_0\Omega_M}{2c} \frac{\chi_l \chi_{sl}(1+z_l)}{\chi_s E(z_l)} & (z_s > z_l), \\ 0 & (z_s \leq z_l). \end{cases} \quad (6)$$

As shown in Kaiser & Squires (1993), the shear distortion is related to the kappa field at the redshift plane as

$$\gamma_L(\vec{\theta}, z_s) = \int d^2\theta' D(\vec{\theta} - \vec{\theta}') \kappa(\vec{\theta}', z_s), \quad (7)$$

where

$$D(\vec{\theta}) = -\frac{1}{\pi}(\theta_1 - i\theta_2)^{-2}. \quad (8)$$

Here we denote the physical shear distortions as γ_L and we note that the observed shear measurements are the physical shear distortions influenced by systematics which will be discussed in the following subsections.

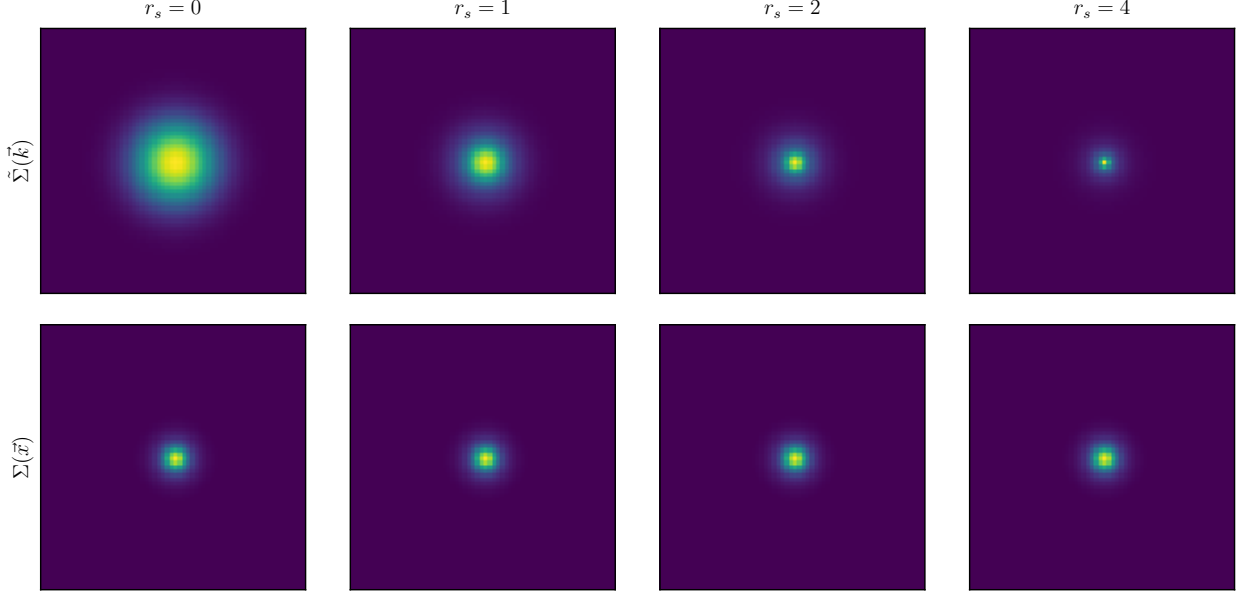


Figure 1. The NFW models with different scale radius (r_s). The first row shows the NFW models in Fourier space and the second row shows the NFW model in Real space.

Combining equation (5) with equation (7), the physical shear signal is derived as

$$\gamma_L(\vec{\theta}, z_s) = \int_0^{z_s} \frac{dz_l}{\delta_c(z_l, z_s)} \int d^2\theta' \vec{D}(\vec{\theta} - \vec{\theta}') \delta(\vec{\theta}', z_l). \quad (9)$$

To simplify the expression, we define the lensing transform operator as

$$\mathbf{Q} = \int_0^{z_s} \frac{dz_l}{\delta_c(z_l, z_s)} \int d^2\theta' \vec{D}(\vec{\theta} - \vec{\theta}'), \quad (10)$$

and eq. (9) is simplified to

$$\gamma_L = \mathbf{Q}\delta. \quad (11)$$

2.2. Dictionary

The density contrast field is modeled as a superposition of basis atoms in the dictionary space $\{\phi_0, \phi_1, \dots, \phi_N\}$.

$$\delta(\vec{r}) = \sum_{s=0}^N \int d^3r' \phi_s(\vec{r} - \vec{r}') x_s(\vec{r}'), \quad (12)$$

where $\phi_s(\vec{r})$ is the basis vector of the dictionary space, and x_s is the corresponding projection coefficients of the density contrast field onto the basis vectors.

These basis vectors are composed of multi-scale NFW atoms $\{\phi_1, \dots, \phi_N\}$ and point mass atoms $\{\phi_0\}$. ϕ_0 is a 3-D Dirac delta function

$$\phi_0(\vec{r}) = \delta_D(\theta_1) \delta_D(\theta_2) \delta_D(z). \quad (13)$$

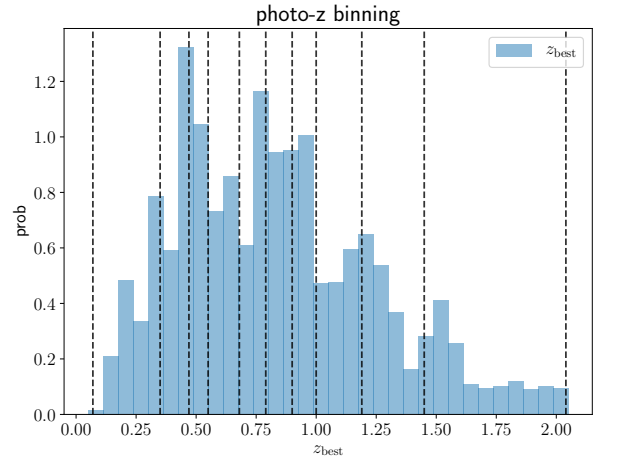


Figure 2. The source galaxies are binned into 10 redshift bins according to their mlz best photo-z estimation. The blue histogram is the number distribution of the best photo-z estimation. The vertical dashed lines are the bounds of bins. The galaxies are evenly distributed in each bins.

on the transverse plane, the NFW atoms ($\{\phi_1, \dots, \phi_N\}$) follow surface density profiles of NFW halos (Takada & Jain 2003) with scale radius θ_α and truncation radius $c\theta_\alpha$, where c is known as concentration of NFW halo. As the scale of halo is much less than the reachable redshift resolution, we neglect the depth of halo on the line-of-sight direction and set the profiles of NFW atoms in the line-of-sight direction to 1-D Dirac delta functions (Leonard et al. 2014). The NFW atoms are expressed

as

$$\phi_\alpha(\vec{r}) = \frac{f}{2\pi\theta_\alpha^2} F(|\vec{\theta}|/\theta_\alpha) \delta_D(z), \quad (14)$$

$$(s = 1..N)$$

where

$$F(x) = \begin{cases} -\frac{\sqrt{c^2-x^2}}{(1-x^2)(1+c)} + \frac{\text{arccosh}\left(\frac{x^2+c}{x(1+c)}\right)}{(1-x^2)^{3/2}} & (x < 1), \\ \frac{\sqrt{c^2-1}}{3(1+c)} \left(1 + \frac{1}{c+1}\right) & (x = 1), \\ -\frac{\sqrt{c^2-x^2}}{(1-x^2)(1+c)} + \frac{\arccos\left(\frac{x^2+c}{x(1+c)}\right)}{(x^2-1)^{3/2}} & (1 < x \leq c), \\ 0 & (x > c). \end{cases} \quad (15)$$

$f = 1/[\ln(1+c) - c/(1+c)]$. In this work, we fix $c = 9$ for NFW atoms in different scale frames.

To simplify the notation, we define the projection pa-

rameters as a column vector: $x = \begin{pmatrix} x_0 \\ x_1 \\ \dots \\ x_N \end{pmatrix}$, and the dic-

tionary transform operator as a row vector:

$$\Phi = \left(\int d^3r \phi_0(\vec{r}) \int d^3r \phi_1(\vec{r}) \dots \int d^3r \phi_N(\vec{r}) \right). \quad (16)$$

We substitute eq. (12) into eq.(9)

$$\gamma_L = \mathbf{Q}\Phi x. \quad (17)$$

Our prior assumption is that the mass density field is sparse in the dictionary space and we will conduct adaptive lasso (Zou 2006) to find a sparse solution of the mass reconstruction problem in the dictionary space.

We note that the shear measurements are deviated from the physical shear prediction due to the systematics from observations. The influence of systematics is carefully studied and added to the forward modeling in the following subsections.

2.3. Systematics

2.3.1. Photo- z Uncertainty

Since the photometric redshifts of source galaxies in the current large scale survey are estimated with a limited number of photometric bands, the estimated redshifts of galaxies suffer from large uncertainties. Such uncertainties smear the structure along the line-of-sight direction since a galaxy with a best fit photo- z estimation of z_s has a possibility of being actually located at redshift z . Such probability is denoted as $P(z|z_s)$ and the expected shear distortion on this galaxy is

$$\gamma_L(\vec{\theta}, z_s) \rightarrow \int dz_s P(z|z_s) \gamma_L(\vec{\theta}, z_s). \quad (18)$$

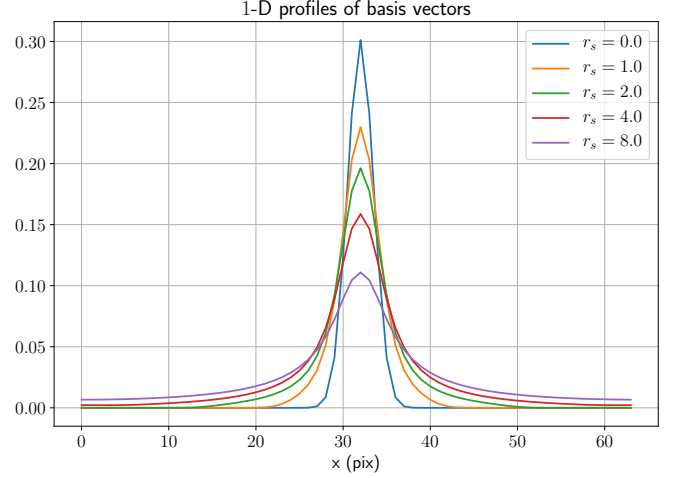


Figure 3. The 1-D slices of NFW models with different scale radius ($r_s = 0, 1, 2, 4, 8$).

With the definition of photo- z smearing operator

$$\mathbf{P} = \int dz_s P(z|z_s), \quad (19)$$

the photo- z uncertainties changes the shear as $\gamma_L \rightarrow \mathbf{Q}\gamma_L$.

2.3.2. Smoothing

The observed galaxies have random irregular (unequally-spaced) spacial distribution. To benefit the computational speed, we smooth the shear measurements from galaxy shapes and pixelise the smoothed measurements onto regular grids.

The smoothing is conducted by convolving the measurements with a smoothing kernel

$$\hat{\gamma} = \frac{\sum_i W(\vec{\theta} - \vec{\theta}_i, z - z_i) e_i}{\sum_i R_i W(\vec{\theta} - \vec{\theta}_i, z - z_i)}, \quad (20)$$

where $W(\vec{\theta}, z)$ is a 3-D smoothing kernel. e_i , R_i , z_i and θ_i are the ellipticity, response, reshift, and transverse position of the ' i -th' galaxy in the galaxy catalog.

$W(\vec{\theta}, z)$ can be decomposed into a transverse component $W_T(\vec{\theta})$ and a line-of-sight component $W_\times(z)$

$$W(\vec{\theta}, z) = W_T(\vec{\theta}) W_\times(z). \quad (21)$$

In this paper, we set

$$W_T(\vec{\theta}) = \frac{1}{2\pi\beta^2} \exp\left(-\frac{|\vec{\theta}|^2}{2\beta^2}\right), \quad (22)$$

$$W_\times(z) = \begin{cases} 1/\Delta z & (|z| < \Delta z/2), \\ 0 & \text{else.} \end{cases}$$

With the approximation that the density of galaxy number vary slowly on the smoothing scale and the fact that $\int d^3r W(\vec{r}) = 1$, the smoothing operator is defined as

$$\mathbf{W} = \int d^3r' W(\vec{r} - \vec{r}'), \quad (23)$$

and the relation between shear signal and projections in the dictionary space is $\gamma_L \rightarrow \mathbf{W}\gamma_L$.

2.3.3. Masking

In the forward modeling, normally the shear field has its prediction on any points within a regular region. However, in real observations, the boundary of the survey, where shear measurements is recorded, is always irregular. Moreover, there are also many regions are masked out due to the existence of neighboring bright stars or bad pixels as bright stars and bad pixels are likely to bias the shape measurements. Therefore, it is necessary to add a mask on the shear field prediction in the forward modeling to match the prediction with realistic observations. The mask changes the shear prediction as follows

$$\gamma_L(\vec{\theta}, z) \rightarrow M(\vec{\theta}, z)\gamma_L(\vec{\theta}, z), \quad (24)$$

$M(\vec{\theta}, z_s)$ is the masking function which is defined as

$$M(\vec{r}) = \begin{cases} 0 & \vec{r} \text{ resides in masked area} \\ 1 & \text{else.} \end{cases} \quad (25)$$

We define the masking operator as

$$\mathbf{M} = \int d^3r' M(\vec{r}')\delta_D(\vec{r} - \vec{r}'), \quad (26)$$

where $\delta_D(\vec{r})$ is 3-D Dirac delta function. The shear is influenced by the masking through $\gamma_L \rightarrow \mathbf{M}\gamma_L$.

The final observed shear field, taking into account all of the aforementioned systematics from observations, is

$$\gamma = \mathbf{MWPQ}\Phi x. \quad (27)$$

For simplicity, we denote $\mathbf{A} = \mathbf{MWPQ}\Phi$ and eq. (27) is written as

$$\gamma = \mathbf{A}x. \quad (28)$$

2.3.4. Pixelization

We pixelize the smoothed shear field into a $N_\theta \times N_\theta \times N_s$ grid, where N_θ is the number of pixels of two orthogonal axes of the transverse plane and N_s is the number of pixels of the line-of-sight axis. γ_α is used to denote the value recorded on pixel with index α , where $\alpha = 1, \dots, N_\theta \times N_\theta \times N_s$. The grid on the transverse plane is equally spaced, therefore Fast Fourier Transform

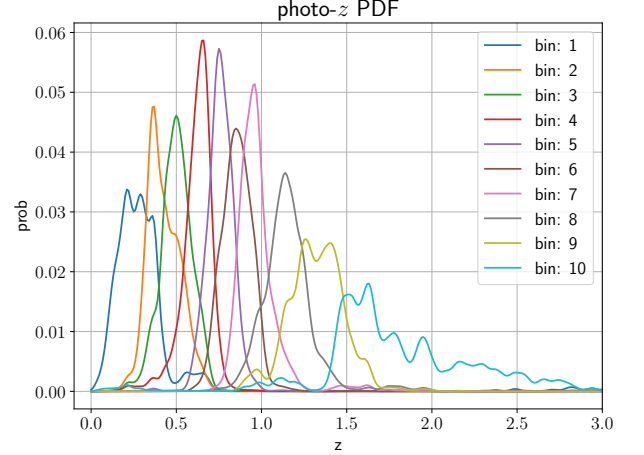


Figure 4. The PDF of photo- z error for 10 source redshift bins.

(FFT) can be used to boost the speed of linear operation on the transverse plan.

Similarly, we pixelize each scale frame of the parameter x into a $N_\theta \times N_\theta \times N_l$ grid. The pixelization of the parameter x on the transverse plan for each scale frame is exactly the same as the pixelization of the smoothed shear field on the transverse plane. N_l is the pixel number of the line-of-sight axis. x_β is used to denote the element of parameter vector x with index β , where $\beta = 1, \dots, N_\theta \times N_\theta \times N_l \times N$. The elements of the forward transform matrix \mathbf{A} is denoted as $A_{\alpha\beta}$.

We term the column vectors of the transform matrix \mathbf{A} as the effective basis vectors. We note that the effective basis vectors have different l^2 norm. The l^2 norm of the i 'th column vectors of the effective basis vectors are $\mathcal{N}_i = \sum_\alpha A_{i\alpha}A_{i\alpha}$. Before solving the density map inversion problem, we normalize the column vectors of the transform matrix through

$$\begin{aligned} A'_{\alpha\beta} &= A_{\alpha\beta}/\mathcal{N}_\alpha^{\frac{1}{2}}, \\ x'_\beta &= x_\beta\mathcal{N}_\beta^{\frac{1}{2}}. \end{aligned} \quad (29)$$

2.4. Density map reversion

2.4.1. Adaptive lasso

The lasso algorithm uses l^1 penalty as the regularization term and the estimator is defined as

$$\hat{x}' = \arg \min_x \left\{ \frac{1}{2} \left\| \Sigma^{-\frac{1}{2}}(\gamma - \mathbf{A}'x') \right\|_2^2 + \lambda \|x'\|_1 \right\}, \quad (30)$$

where $\|\cdot\|_1$ and $\|\cdot\|_2$ refer to the l^1 norm and l^2 norm, respectively. The l^p norm is defined as

$$\|x'\|_p = \left(\sum_i |x'_i|^p \right)^{\frac{1}{p}}. \quad (31)$$

Given that the parameters to measure is sparse in the parameter space, the lasso algorithm can select the parameters which are relevant to the measurements and simultaneously estimate the value of the selected parameters. However, it has been shown by Zou (2006) that when the column vectors of \mathbf{A}' are highly correlated, lasso cannot select the related parameters from the parameter space consistently. Moreover, the estimated parameters are biased due to the shrinkage process in the lasso regression.

Zou (2006) proposes the adaptive lasso algorithm which uses adaptive weights to penalize different coefficients in the l^1 penalty. The adaptive lasso algorithm is a two-steps process. Lasso estimation is performed in the first step and achieve a preliminary lasso estimation of parameter (\hat{x}'^{lasso}). In the second step, the lasso estimation is used to weight the penalization on the parameters. With the definition of the adaptive lasso weight

$$\hat{w} = \frac{1}{\left| \hat{x}'^{\text{lasso}} \right|^\tau}, \quad (32)$$

here we set the hyper-parameter τ to 2, the adaptive lasso estimator is expressed as

$$\hat{x}' = \arg \min_{x'} \left\{ \frac{1}{2} \left\| \Sigma^{-\frac{1}{2}} (\gamma - \mathbf{A}' x') \right\|_2^2 + \hat{w} \lambda \|x'\|_1 \right\}. \quad (33)$$

The loss function can be rewritten with Einstein notation

$$L(x') = \frac{1}{2} (\Sigma^{-1})_{\alpha\beta} (\gamma_\alpha^* - A'_{\alpha i} x'_i) (\gamma_\beta - A'_{\beta j} x'_j) + \lambda \hat{w}_\beta |x'_\beta|. \quad (34)$$

To simplify the notification, we define the quadruple term in the loss function as $G(x')$:

$$G(x') = \frac{1}{2} \Sigma_{\alpha\beta}^{-1} (\gamma_\alpha^* - A'_{\alpha i} x'_i) (\gamma_\beta - A'_{\beta j} x'_j). \quad (35)$$

2.4.2. FISTA

In this work, we apply the Fast Iterative Soft Thresholding Algorithm (FISTA) of Beck & Teboulle (2009) to solve the adaptive lasso estimator.

The parameter vector is initialized as $x^{(1)} = 0$. According to the FISTA algorithm, we iteratively update the elements of the parameter vector (x). In the n 'th iteration, a temporary update is first calculated as

$$x'_i{}^{(n+1)} = \text{ST}_\lambda \left(x'_i{}^{(n)} - \mu \partial_i G(x'^{(n)}) \right), \quad (36)$$

where ST is the soft thresholding function defined as

$$\text{ST}_\lambda (x') = \text{sign}(x') \max(|x'| - \lambda, 0). \quad (37)$$

μ is the step size of the gradient descent iteration. $\partial_i G(x'^{(n)})$ refers to the i 'th element of the gradient vector of G at point $x'^{(n)}$

$$\partial_i G(x'^{(n)}) = \Sigma_{\alpha\beta}^{-1} \text{Re} \left(A'_{\alpha i}^* (\gamma_\beta - A'_{\beta j} x'_j) \right), \quad (38)$$

where $\text{Re}(\bullet)$ is the function returns the real part of the input function. The FISTA algorithm requires an additional step amounting to a weighted average between $x'^{(n+1)}$ and $x'^{(n)}$:

$$t^{(n+1)} = \frac{1 + \sqrt{1 + 4(t^{(n)})^2}}{2}, \quad (39)$$

$$x'_{n+1} \leftarrow x'^{(x+1)} + \frac{t^{(n)} - 1}{t^{(n+1)}} (x'^{(n+1)} - x'^{(n)}),$$

where the relative weight is initialized as $t^{(1)} = 1$.

Note that the FISTA algorithm converges as long as the gradient descent step size μ satisfies

$$0 < \mu < \frac{1}{\|\mathbf{A}^\dagger \Sigma^{-1} \mathbf{A}\|}, \quad (40)$$

where $\|\mathbf{A}^\dagger \Sigma^{-1} \mathbf{A}\|$ refers to the spectrum norm of the matrix $\mathbf{A}^\dagger \Sigma^{-1} \mathbf{A}$. The spectral norm is estimated using random vectors. We simulate large number of random vectors with l^2 norms equal one with different realizations. Then, the matrix $\mathbf{A}^\dagger \Sigma^{-1} \mathbf{A}$ is applied to each random vector and get a corresponding transformed random vector. The spectral norm of the matrix $\mathbf{A}^\dagger \Sigma^{-1} \mathbf{A}$ is the maximum l^2 norm of the transformed vectors.

2.4.3. The Algorithm

The algorithm is described in Algorithm 2.4.3.

Algorithm Our Algorithm

Input: γ : Pixelized complex 3-D array of shear

Output: δ : 3-D array of density contrast

1: Normalize column vectors of \mathbf{A}

2: Estimate step size μ and Σ

3: **Initialization:**

4: $x'^{(1)} = 0$

5: $\hat{w} = 1$

6: $t^{(1)} = 1, i = 1, j = 1$

7: **while** $j \leq 2$ **do**

8: **while** $i \leq N_{\text{iter}}$ **do**

9: $x'_i{}^{(n+1)} = \text{ST}_{\hat{w}\lambda} \left(x'_i{}^{(n)} - \mu \partial_i G(x'^{(n)}) \right)$

10: $t^{(n+1)} = \frac{1 + \sqrt{1 + 4(t^{(n)})^2}}{2}$

11: $x'_{n+1} \leftarrow x'^{(x+1)} + \frac{t^{(n)} - 1}{t^{(n+1)}} (x'^{(n+1)} - x'^{(n)})$

12: **end while**

13: **Reinitialization:**

14: $\hat{w} \leftarrow \left| \hat{x}'^{\text{lasso}} \right|^{-2}$

15: $\hat{x}'^{(1)} \leftarrow x'^{(N_{\text{iter}})}$

16: $t^{(1)} \leftarrow 1, i \leftarrow 1$

17: **end while**

18: $\delta = \Phi \mathcal{N}^{-\frac{1}{2}} x'^{(N_{\text{iter}})}$

3. SIMULATION

This section simulates lensing shear fields induced by a group of dark matter halos with various halo mass and redshifts. HSC-like shape measurement error and photo- z error are added to the shear field.

3.1. Weak Lensing Fields

We simulate weak lensing shear fields of NFW halos according to Takada & Jain (2003) and sample halos in the mass-redshift plane as shown in Figure 6. We assume a dependency of the concentration on the mass and the redshift of a halo as (Ragagnin et al. 2019)

$$c_h = 6.02 \times \left(\frac{M_{200}}{10^{13} M_\odot}\right)^{-0.12} \left(\frac{1.47}{1+z_h}\right)^{0.16}. \quad (41)$$

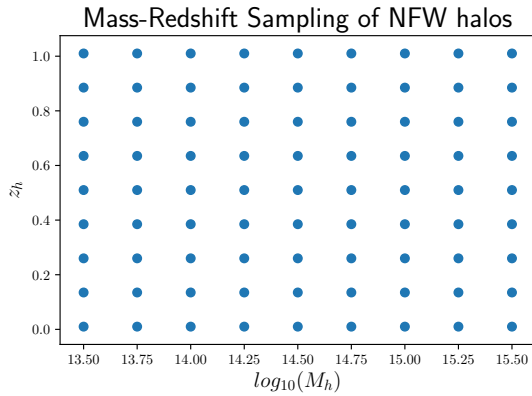


Figure 5. The sampling points of halos in the mass-redshift plane.

3.2. HSC-like Systematic

3.2.1. Shear Measurement Error

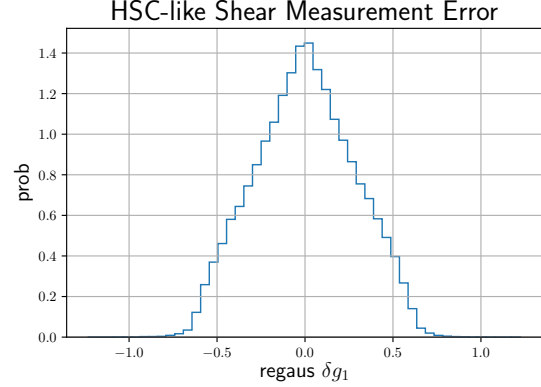


Figure 6. HSC-like measurement error on the first component of shear (g_1).

3.2.2. Photo- z Error

4. RESULTS

4.1. Detection

4.2. Redshift

4.3. Density Map

5. SUMMARY

REFERENCES

- Aihara, H., Armstrong, R., Bickerton, S., et al. 2018, PASJ, 70, S8, doi: [10.1093/pasj/psx081](https://doi.org/10.1093/pasj/psx081)
- Beck, A., & Teboulle, M. 2009, SIAM Journal on Imaging Sciences, 2, 183
- Chang, C., Pujol, A., Mawdsley, B., et al. 2018, MNRAS, 475, 3165, doi: [10.1093/mnras/stx3363](https://doi.org/10.1093/mnras/stx3363)
- de Jong, J. T. A., Kuijken, K., Applegate, D., et al. 2013, The Messenger, 154, 44
- Hamana, T., Shirasaki, M., Miyazaki, S., et al. 2020, PASJ, 72, 16, doi: [10.1093/pasj/psz138](https://doi.org/10.1093/pasj/psz138)
- Han, J., Eke, V. R., Frenk, C. S., et al. 2015, MNRAS, 446, 1356, doi: [10.1093/mnras/stu2178](https://doi.org/10.1093/mnras/stu2178)
- Hikage, C., Oguri, M., Hamana, T., et al. 2019, PASJ, 71, 43, doi: [10.1093/pasj/psz010](https://doi.org/10.1093/pasj/psz010)
- Jeffrey, N., Abdalla, F. B., Lahav, O., et al. 2018, MNRAS, 479, 2871, doi: [10.1093/mnras/sty1252](https://doi.org/10.1093/mnras/sty1252)
- Kaiser, N., & Squires, G. 1993, pj, 404, 441, doi: [10.1086/172297](https://doi.org/10.1086/172297)
- Kilbinger, M. 2015, Reports on Progress in Physics, 78, 086901, doi: [10.1088/0034-4885/78/8/086901](https://doi.org/10.1088/0034-4885/78/8/086901)
- Lanusse, F., Starck, J. L., Leonard, A., & Pires, S. 2016, ap, 591, A2, doi: [10.1051/0004-6361/201628278](https://doi.org/10.1051/0004-6361/201628278)
- Laureijs, R., Amiaux, J., Arduini, S., et al. 2011, ArXiv e-prints. <https://arxiv.org/abs/1110.3193>
- Leonard, A., Lanusse, F., & Starck, J.-L. 2014, MNRAS, 440, 1281, doi: [10.1093/mnras/stu273](https://doi.org/10.1093/mnras/stu273)
- LSST Science Collaboration, Abell, P. A., Allison, J., et al. 2009, ArXiv e-prints. <https://arxiv.org/abs/0912.0201>
- Mandelbaum, R. 2018, ARA&A, 56, 393, doi: [10.1146/annurev-astro-081817-051928](https://doi.org/10.1146/annurev-astro-081817-051928)

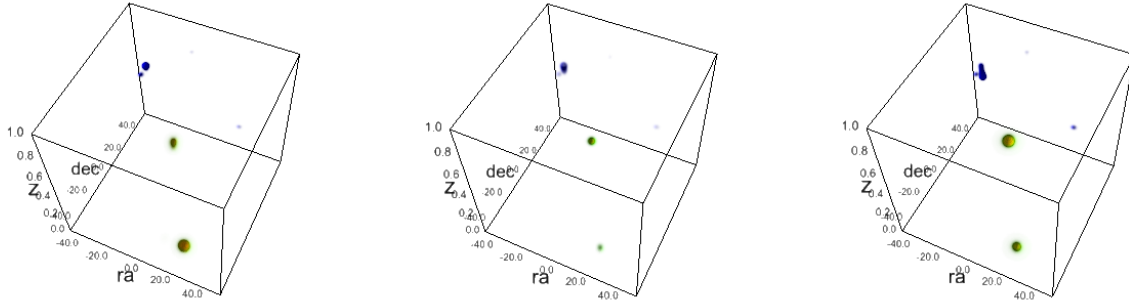


Figure 7. The density map reconstructed for a halo with mass= $3.16 \times 10^{14} M_{\odot}/h$, $z = 0.51$. The left panel shows the results with $\tau = 0.10$, the middle panel is the result for $\tau = 0.15$, the right panel is for $\tau = 0.20$.

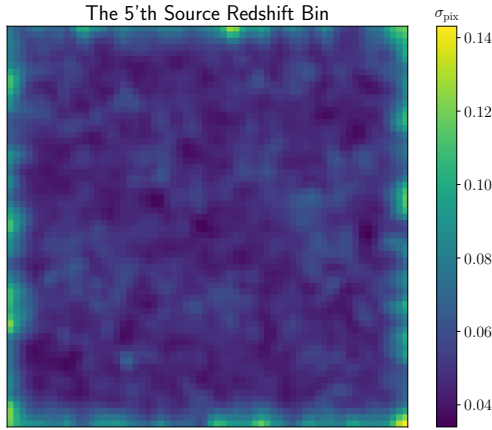


Figure 8. The standard deviation map of shear measurement error for the fifth source bin ($0.69 \leq z < 0.80$).

More, S., Miyatake, H., Mandelbaum, R., et al. 2015, *The Astrophysical Journal*, 806, 2,
doi: [10.1088/0004-637x/806/1/2](https://doi.org/10.1088/0004-637x/806/1/2)

Morrison, C. B., Klaes, D., van den Busch, J. L., et al. 2016, *Monthly Notices of the Royal Astronomical Society*, 465, 1454, doi: [10.1093/mnras/stw2805](https://doi.org/10.1093/mnras/stw2805)

Navarro, J. F., Frenk, C. S., & White, S. D. M. 1997, *pj*, 490, 493, doi: [10.1086/304888](https://doi.org/10.1086/304888)

Oguri, M., Miyazaki, S., Hikage, C., et al. 2018, *PASJ*, 70, S26, doi: [10.1093/pasj/psx070](https://doi.org/10.1093/pasj/psx070)

Prat, J., Sánchez, C., Fang, Y., et al. 2018, *Phys. Rev. D*, 98, 042005, doi: [10.1103/PhysRevD.98.042005](https://doi.org/10.1103/PhysRevD.98.042005)

Ragagnin, A., Dolag, K., Moscardini, L., Biviano, A., & D'Onofrio, M. 2019, *MNRAS*, 486, 4001, doi: [10.1093/mnras/stz1103](https://doi.org/10.1093/mnras/stz1103)

Simon, P., Taylor, A. N., & Hartlap, J. 2009, *MNRAS*, 399, 48, doi: [10.1111/j.1365-2966.2009.15246.x](https://doi.org/10.1111/j.1365-2966.2009.15246.x)

Spergel, D., Gehrels, N., Baltay, C., et al. 2015, *ArXiv e-prints*. <https://arxiv.org/abs/1503.03757>

Takada, M., & Jain, B. 2003, *MNRAS*, 340, 580, doi: [10.1046/j.1365-8711.2003.06321.x](https://doi.org/10.1046/j.1365-8711.2003.06321.x)

The Dark Energy Survey Collaboration. 2005, *ArXiv Astrophysics e-prints*

Troxel, M. A., MacCrann, N., Zuntz, J., et al. 2018, *Phys. Rev. D*, 98, 043528, doi: [10.1103/PhysRevD.98.043528](https://doi.org/10.1103/PhysRevD.98.043528)

Zou, H. 2006, *Journal of the American Statistical Association*, 101, 1418, doi: [10.1198/016214506000000735](https://doi.org/10.1198/016214506000000735)

APPENDIX